



















## Investigating Protostellar Accretion across the mass spectrum with the JWST: discovery of a collimated jet from the low luminosity protostar IRAS 16253-2429 in a quiescent accretion phase

MAYANK NARANG <sup>1,2</sup> P. MANOJ <sup>2</sup> HIMANSHU TYAGI <sup>2</sup> DAN M. WATSON <sup>3</sup> S. THOMAS MEGEATH <sup>4</sup>  
SAMUEL FEDERMAN <sup>4</sup> ADAM E. RUBINSTEIN <sup>3</sup> ROBERT GUTERMUTH <sup>5</sup> ALESSIO CARATTI O GARATTI <sup>6</sup>  
HENRIK BEUTHER <sup>7</sup> TYLER L. BOURKE <sup>8</sup> EWINE F. VAN DISHOECK <sup>9,10</sup> NEAL J. EVANS II <sup>11</sup>  
GUILLEM ANGLADA <sup>12</sup> MAYRA OSORIO <sup>12</sup> THOMAS STANKE <sup>10</sup> JAMES MUZEROLLE <sup>13</sup> LESLIE W. LOONEY <sup>14,15</sup>  
YAO-LUN YANG <sup>16</sup> PAMELA KLAASSEN <sup>17</sup> NICOLE KARNATH <sup>18,19</sup> PRABHANI ATNAGULOV <sup>20</sup>  
NASHANTY BRUNKEN <sup>9</sup> WILLIAM J. FISCHER <sup>21</sup> ELISE FURLAN <sup>22</sup> JOEL GREEN <sup>21</sup> NOLAN HABEL <sup>23</sup>  
LEE HARTMANN <sup>24</sup> HENDRIK LINZ <sup>7,25</sup> RIWAJ POKHREL <sup>20</sup> ROHAN RAHATGAONKAR <sup>26</sup> WILL R. M. ROCHA <sup>27</sup>  
PATRICK SHEEHAN <sup>15</sup> KATERINA SLAVICINSKA <sup>9</sup> AMELIA M. STUTZ <sup>28</sup> JOHN J. TOBIN <sup>15</sup> LUKASZ TYCHONIEC <sup>29</sup>  
AND SCOTT WOLK <sup>19</sup>

<sup>1</sup>Academia Sinica Institute of Astronomy & Astrophysics, 11F of Astro-Math Bldg., No.1, Sec. 4, Roosevelt Rd., Taipei 10617, Taiwan, R.O.C.

<sup>2</sup>Department of Astronomy and Astrophysics Tata Institute of Fundamental Research  
Homi Bhabha Road, Colaba, Mumbai 400005, India

<sup>3</sup>University of Rochester, Rochester, NY, US

<sup>4</sup>University of Toledo, Toledo, OH, US

<sup>5</sup>University of Massachusetts Amherst, Amherst, MA, US

<sup>6</sup>INAF-Osservatorio Astronomico di Capodimonte, IT

<sup>7</sup>Max Planck Institute for Astronomy, Heidelberg, Baden Wuerttemberg, DE

<sup>8</sup>SKA Observatory, Jodrell Bank, Lower Withington, Macclesfield SK11 9FT, UK

<sup>9</sup>Leiden Observatory, Universiteit Leiden, Leiden, Zuid-Holland, NL

<sup>10</sup>Max-Planck Institut für Extraterrestrische Physik, Garching bei München, DE

<sup>11</sup>Department of Astronomy, The University of Texas at Austin, 2515 Speedway, Stop C1400, Austin, Texas 78712-1205, USA

<sup>12</sup>Instituto de Astrofísica de Andalucía (IAA-CSIC), Granada, Andalucía, ES

<sup>13</sup>Space Telescope Science Institute, Baltimore, MD, US

<sup>14</sup>Department of Astronomy, University of Illinois, 1002 West Green St, Urbana, IL 61801, USA

<sup>15</sup>National Radio Astronomy Observatory, 520 Edgemont Rd., Charlottesville, VA 22903 USA

<sup>16</sup>RIKEN Cluster for Pioneering Research, Wako-shi, Saitama, 351-0106, Japan

<sup>17</sup>United Kingdom Astronomy Technology Centre, Edinburgh, GB

<sup>18</sup>Space Science Institute, Boulder, CO, US

<sup>19</sup>Center for Astrophysics Harvard & Smithsonian, Cambridge, MA, US

<sup>20</sup>Ritter Astrophysical Research Center, Dept. of Physics and Astronomy, University of Toledo, Toledo, OH, US

<sup>21</sup>Space Telescope Science Institute, 3700 San Martin Drive, Baltimore, MD 21218, US

<sup>22</sup>Caltech/IPAC, Pasadena, CA, US

<sup>23</sup>Jet Propulsion Laboratory, Pasadena, CA, US

<sup>24</sup>University of Michigan, Ann Arbor, MI, US

<sup>25</sup>Friedrich-Schiller-Universität, Jena, Thüringen, DE

<sup>26</sup>Gemini South Observatory, La Serena, CL

<sup>27</sup>Laboratory for Astrophysics, Leiden Observatory, Universiteit Leiden, Leiden, Zuid-Holland, NL

<sup>28</sup>Departamento de Astronomía, Universidad de Concepción, Casilla 160-C, Concepción, Chile

<sup>29</sup>European Southern Observatory, Garching bei München, DE

### ABSTRACT

Investigating Protostellar Accretion (IPA) is a JWST Cycle 1 GO program that used NIRSpec IFU and MIRI MRS to obtain 2.9–28  $\mu\text{m}$  spectral cubes of young, deeply embedded, protostars with luminosities of 0.2 to 10,000  $L_{\odot}$  and central masses of 0.15 to 12  $M_{\odot}$ . In this Letter, we report the discovery of a highly collimated atomic jet from the Class 0 protostar IRAS 16253-2429, the lowest luminosity (mass) source in the IPA program. The collimated jet is clearly detected in multiple [Fe II] lines, [Ne II], [Ni II], and H I lines, but not in molecular emission. From our analysis, we find that the atomic jet has a velocity of about  $169 \pm 15 \text{ km s}^{-1}$ , after correcting for inclination. The width of the jet

increases with distance from the central protostar from 23 to 60 au, corresponding to an opening angle of  $2.6 \pm 0.5^\circ$ . By comparing the measured flux ratios of various fine structure lines to those predicted by simple shock models, we derive a shock velocity of  $54 \text{ km s}^{-1}$  and a preshock density of  $2.0 \times 10^3 \text{ cm}^{-3}$  at the base of the jet. From these quantities, and assuming a cylindrical cross-section for the jet, we derive an upper limit for the mass loss rate from the protostar of  $1.1 \times 10^{-10} M_\odot \text{ yr}^{-1}$ . The low mass loss rate is consistent with simultaneous measurements of low mass accretion rate ( $\sim 1.3 \times 10^{-9} M_\odot \text{ yr}^{-1}$ ) for IRAS 16253-2429 from JWST observations (Watson et al. in prep), indicating that the protostar is in a quiescent accretion phase. Our results demonstrate that very low-mass protostars can drive highly collimated, atomic jets, even during the quiescent phase.

## 1. INTRODUCTION

Jets and outflows from protostars and pre-main sequence stars play a crucial role in the process of star formation. These dynamic phenomena are instrumental in facilitating the removal of angular momentum from the surrounding disk material, thereby enabling efficient accretion of mass onto the central object (e.g., Shang et al. 2007; Pudritz et al. 2007; Hartmann et al. 2016; Frank et al. 2014; Bally 2016; Ray & Ferreira 2021). These accretion-driven outflows/jets also play vital roles in shaping the Initial Mass Function (IMF) (e.g., Bate 2009; Hennebelle et al. 2020; Appel et al. 2023) and can inject energy and momentum into the surroundings, and disperse a significant fraction of the protostellar envelope, which limits star formation efficiency (e.g., Bate 2009; Fall et al. 2010; Hennebelle et al. 2020; Frank et al. 2014).

Despite their unquestionable significance, the precise origins of protostellar jets and outflows remain uncertain and continue to be a subject of debate. Among the various proposed mechanisms, the most widely accepted one is the magnetocentrifugal acceleration (Blandford & Payne 1982; Pudritz & Norman 1983; Pelletier & Pudritz 1992; Wardle & Koenigl 1993; Najita & Shu 1994; Shu et al. 1994; Matt & Pudritz 2005, 2008; Frank et al. 2014). According to this model, material situated near the surface of the inner parts of the disk is ejected centrifugally along the rotating magnetic field lines. As the outflow progresses beyond the so-called “Alfvén surface,” where the kinetic energy matches the magnetic energy, the dynamics begin to dominate over the magnetic field, resulting in a predominantly toroidal magnetic configuration. The tension force generated by these magnetic loops focuses the outflowing material into a narrow jet along the rotational axis of the circumstellar disk that originally launched the (MHD) wind (Blandford & Payne 1982; Spruit 1996; Ray & Ferreira 2021). As a result, highly collimated bipolar jets are formed.

The three classes of models that are most successful in explaining the launching of outflows from YSOs are X-wind, the disk-wind, and accretion-powered stel-

lar winds. In the X-wind model (e.g. Shu et al. 1988, 2000), the jet-launching magnetic field is concentrated near the inner edge of the disk, known as the “X-point,” where the stellar magnetosphere truncates the disk. The disk-wind model (e.g. Pelletier & Pudritz 1992; Pudritz et al. 2007) posits that the outflow-launching field lines (threaded through the disk) extend over a broader range of larger disk radii (also see Lee et al. 2022). In the accretion-powered stellar wind scenario (e.g., Matt & Pudritz 2005, 2008), a fraction of the energy released by mass accreting onto the protostar powers the stellar wind (also see Watson et al. 2016). Though all these models predict that the mass ejection rate is proportional to the mass accretion rate, the constant of proportionality depends upon the underlying model (Watson et al. 2016). Therefore to better understand the launching of the jets/outflow from protostars, it is critically important to study the mass ejection and accretion rates from them.

Infrared emission lines of [Fe II] and  $\text{H}_2$  are well-known tracers of shocked gas and have been used to trace outflows and jets from protostars (e.g. Caratti o Garatti et al. 2006; Agra-Amboage et al. 2014; Reipurth et al. 2019; Watson et al. 2016; Bally 2016; Yang et al. 2022; Beuther et al. 2023; Harsono et al. 2023; Rubinstein et al. 2023; Ray, T. P. et al. 2023). These lines serve as excellent diagnostics for deriving the physical conditions of the collimated jets as well as the shocked molecular gas in the outflow (Ray, T. P. et al. 2023). Therefore by harnessing the spatial and spectral resolution as well as the sensitivity of JWST, we can gain a deeper understanding of the launching of and feedback from the protostellar outflows/jets.

Investigating Protostellar Accretion (IPA) across the mass spectrum is a JWST Cycle 1 medium GO program (Program ID 1802, PI Tom Megeath; Megeath et al. 2021, Federman et al. 2023b Rubinstein et al., in prep, Watson et al., prep). The IPA program aims to study the processes that drive protostellar accretion, and accretion-driven jets/outflows as a function of protostellar mass. The program also aims to characterize the chemical and spatial variation of ices in the sur-

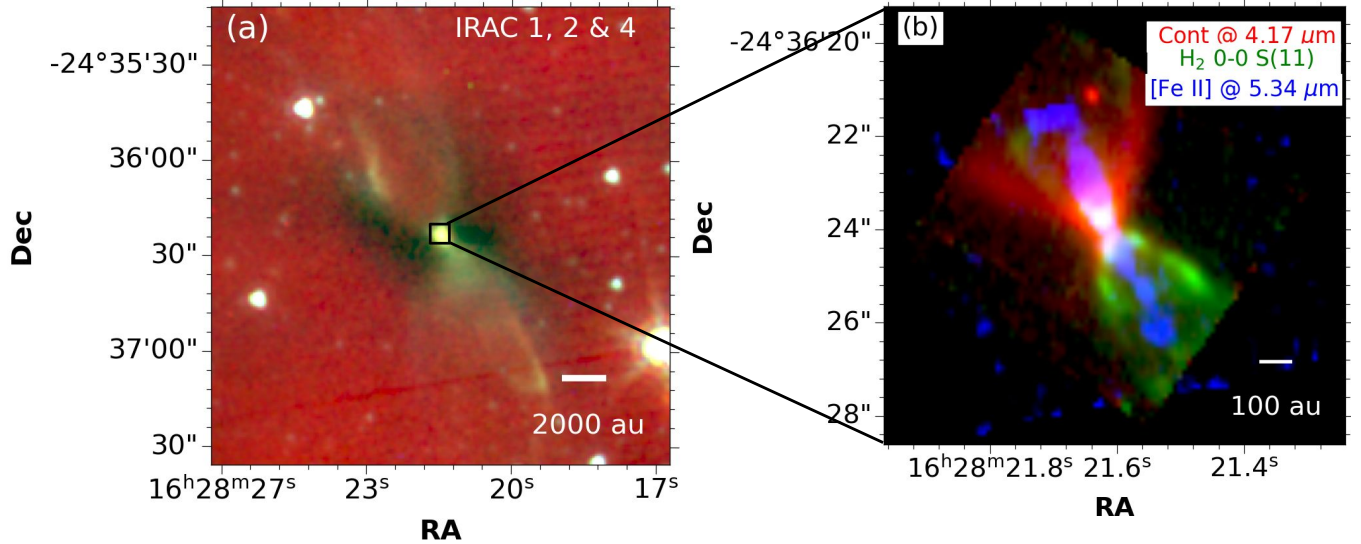


**Figure 1.** (a) The Spitzer IRAC 3 color (IRAC 1, 2, and 4 are R G B respectively) image of the IRAS 16253-2429 field. The field of view is  $2' \times 2'$ . The black square in the center represents the JWST FOV. (b) A zoomed-in view of the NIRSpect and MIRI channel-1 short field with the red representing continuum emission at  $4.17 \mu\text{m}$ , the green showing  $\text{H}_2$  0-0 S(11) at  $4.18 \mu\text{m}$  and the blue depicting [Fe II] at  $5.34 \mu\text{m}$ . A local continuum has been subtracted to make the line maps.

**Table 1.** The log of our JWST observations.

Observation	RA	Dec	Hours	Start UT	End UT
NIRSpect IFU IRAS 16253-2429	16 28 21.6200	-24 36 24.16	3.43	Jul 22, 2022 15:09:15	Jul 22, 2022 17:59:43
MIRI MRS IRAS 16253-2429	16 28 21.6200	-24 36 24.16	7.43	Jul 23, 2022 04:04:41	Jul 23, 2022 09:58:57
MIRI MRS IRAS 16253-2429 background	16 28 27.7560	-24 37 46.95	1.86	Jul 23, 2022 10:02:33	Jul 23, 2022 11:35:19

rounding protostellar envelope (Brunken et al., in prep, Tyagi et al., in prep, Nazari et al., in prep and Slavicinska et al., in prep). To achieve this, the IPA program utilizes the NIRSpect+MIRI Integral Field Units (IFUs) to obtain spectral cubes spanning the wavelength range of  $2.9\text{-}28 \mu\text{m}$ . The IPA protostellar sample consists of five sources that range in bolometric luminosities from 0.2 to  $10,000 L_{\odot}$  and in central masses from 0.15 to  $12 M_{\odot}$ . These protostars are in the Class 0 phase, during which most of the stellar mass is accreted (e.g., Fischer et al. 2017; Narang et al. 2023).

The protostar IRAS 16253-2429 is the lowest mass and lowest luminosity source in the IPA sample. It is located in a relatively isolated region of the  $\rho$ -Ophiuchus molecular cloud (Khanzadyan et al. 2004; Stanke et al. 2006; Barsony et al. 2010). With a bolometric luminosity of only  $0.2 L_{\odot}$  and a bolometric temperature of 42 K (Pokhrel et al., in preparation; also see Pokhrel et al. 2023), coupled with an internal luminosity below  $0.15 L_{\odot}$  (Pokhrel et al., in preparation), IRAS 16253-2429 falls under the category of a very low luminosity object (VeLLO) (Dunham et al. 2008). Being only at a distance

of 140 pc (average of  $\rho$ -Ophiuchi molecular cloud members Zucker et al. 2020) and relatively isolated, IRAS 16253-2429 is an ideal target to study the morphology and kinematics of jets from very low mass ( $< 0.2 M_{\odot}$ ) protostars.

Extensive studies have been conducted on this protostar, particularly at the (sub)millimeter wavelengths (Stanke et al. 2006; Tobin et al. 2011; Yen et al. 2017; Hsieh et al. 2019). These observations have revealed the presence of a central protostar associated with a bipolar outflow identified in CO, as well as a Keplerian disk. However, no collimated molecular jet in CO or SiO has been detected from the system (Aso et al. 2023). This is consistent with the low detection rate of molecular jets from low luminosity protostars (e.g., Podio et al. 2021). Recent observations with ALMA have estimated the dynamical mass of the central source to be between  $0.12\text{-}0.17 M_{\odot}$  (Aso et al. 2023), indicating that IRAS 16253-2429 has already accreted a mass above the hydrogen-burning limit. The protostar also has a tiny disk with a radius of  $16 \pm 3 \text{ au}$  (Aso et al. 2023) with a mass of  $\sim 2 \times 10^{-3} M_{\odot}$ . The envelope mass of IRAS 16253-2429

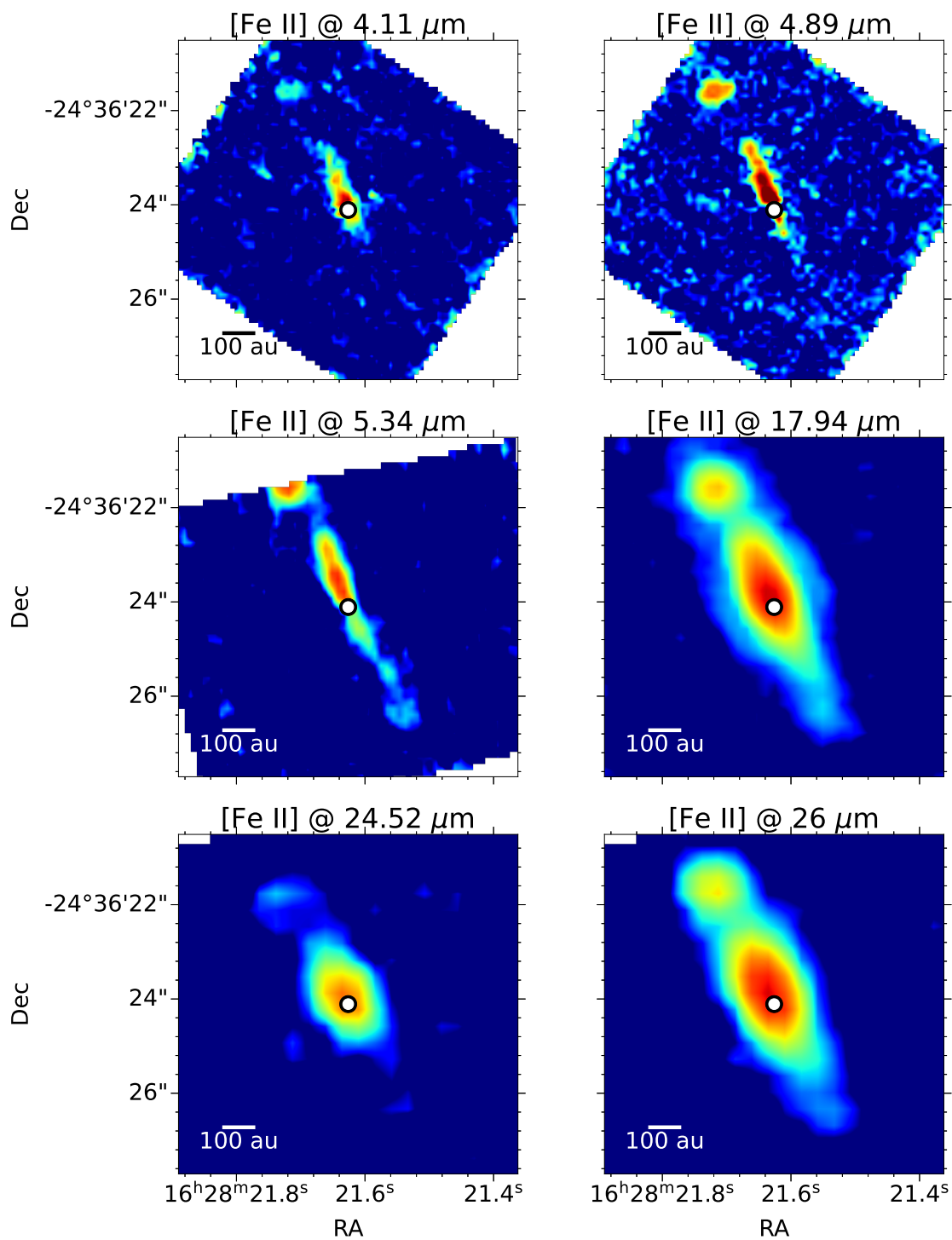


**Figure 2.** The morphology of [Fe II] lines detected towards IRAS 16253-2429. All these lines trace the collimated jet launched from the protostar. All images are cropped to the same spatial scale. The white solid circle is the MIRI MRS 14  $\mu\text{m}$  continuum position. The scale bar corresponding to 100 au is shown in the bottom left corner.

also has been estimated from mm observations are in the range of 0.2 to 1  $M_{\odot}$  (Stanke et al. 2006; Enoch et al. 2008; Tobin et al. 2011). The disk-to-envelope mass ratio for IRAS 16253-2429 therefore is  $\ll 0.01$  and is consistent with the values reported for Class 0 protostars by Federman et al. (2023a).

Figure 1 shows the Spitzer Infrared Array Camera (IRAC) images of the IRAS 16253-2429 field, which reveal a bipolar hourglass structure in the Northeast to Southwest direction. This distinctive shape is traced by the outflow cavities in  $H_2$  and the continuum. The bipolar outflow from the source extends up to 2' in size, corresponding to a physical scale of 16800 AU or 0.08 pc. In addition to the imaging, the Spitzer IRS instrument also carried out spectral scan mapping of the protostar (Barsony et al. 2010). The Spitzer IRS spectra detected six pure rotational  $H_2$  (0-0 S(2) to 0-0 S(7)) lines along the protostellar outflow. However, no fine structure lines were detected from the protostar with Spitzer/IRS.

## 2. OBSERVATIONS AND DATA REDUCTION

Our primary objective with the JWST observations was to perform spectral imaging by combining the Integral Field Unit (IFU) observations from the Mid-Infrared Instrument (MIRI) Medium Resolution Spectrograph (MRS) (Rieke et al. 2015; Wright et al. 2015) and the Near Infrared Spectrograph (NIRSpec) (Jakobsen et al. 2022; Böker et al. 2022) covering from 2.87 to 28  $\mu\text{m}$ . The NIRSpec IFU and MIRI MRS observations were conducted near-simultaneously. The details of the observation log are provided in Table 1.

For the NIRSpec IFU observations, we utilized the F290L/G395M filter/grating combination. To ensure comprehensive coverage, we employed a  $2 \times 2$  mosaic pattern with a 10% overlap and a 4-point dither mode. The NIRSpec field of view (FOV) is  $\sim 6'' \times 6''$ . The total exposure time, which accounted for overheads, amounted to 3.43 hours (for further detail, see Federman et al. 2023b).

IRAS 16253-2429 was observed using all four channels of the MIRI MRS. Similar to the NIRSpec observations, we employed a  $2 \times 2$  mosaic pattern with a 10% overlap and a 4-point dither for the MIRI observations. The total exposure time, including overheads, for the science target amounted to 7.43 hours. Additionally, a dedicated background observation with a similar setup and an exposure time of 1.86 hours (including overheads) was obtained. The dedicated background field was positioned approximately 118'' away from the target. The field of view (FOV) for MIRI varies from channel to channel with channel-1 short covering a FOV of  $\sim 6'' \times 6''$  while for channel-4 long the FOV is  $\sim 15'' \times 15''$ . The

orientation and FOV of the MIRI MRS is also different from NIRSpec IFU.

We reduced the NIRSpec IFU using the JWST pipeline version 1.9.5 and the JWST Calibration References Data System context version `jwst_1069.pmap`. Our analysis of the NIRSpec data showed the presence of several hot pixels that were being missed by the JWST outlier detection step. These hot pixels were a function of both wavelengths as well as time. Hence a universal dark mask could not be used. To remedy this, we used a custom outlier detection algorithm for the NIRSpec observations to remove the hot pixels (see Federman et al. 2023b). In addition, MIRI parallel imaging observations were obtained at both MIRI pointings.

To reduce the MIRI data we used the JWST pipeline version 1.11.3 and the JWST Calibration References Data System context version `jwst_1100.pmap`. We used the standard Stage-1 JWST pipeline *Detector1Pipeline* to reduce the MIRI MRS data starting from *uncal* data. In Stage-2 (*Spec2Pipeline*), the dedicated background was subtracted, and the residual fringe correction was also performed. The Stage-3 *Spec3Pipeline* step was then run with the *CubeBuildStep* set to 'band' mode such that each channel and each band are reduced as a separate fits file. However, on examining the dedicated background IFU image, we detected emission from the  $H_2$  S (1) (17.035  $\mu\text{m}$ ) and  $H_2$  S(2) (12.279  $\mu\text{m}$ ) molecular lines. Therefore we also reduced the MIRI MRS data without subtracting the dedicated background. We will use these non-background subtracted data cubes for measuring the extinction in Section 3.3.

During our analysis of the data obtained from the MIRI MRS and NIRSpec IFU instruments, we found a positional offset between the two instruments. To accurately determine and quantify this offset between the two instruments, we focused on the overlapping region of MIRI MRS channel 1-short and the NIRSpec IFU. The positional offset between these two instruments was  $\Delta\text{RA} = 0.37''$  and  $\Delta\text{Dec} = 0.67''$ . We also refined the position of the MIRI MRS field by aligning it with Spitzer and Gaia data of the stellar sources detected in the MIRI parallel image. Thus we aligned the NIRSpec and MIRI spectral images before carrying out our analysis. For further elaboration and in-depth information concerning this positional offset see Narang et al., (in prep) and Federman et al. (2023b).

## 3. JET FROM IRAS 16253-2429

### 3.1. Morphology

The observations of IRAS 16253-2429 carried out with the JWST NIRSpec IFU and MIRI MRS instruments provide valuable insights about the protostar, reveal-

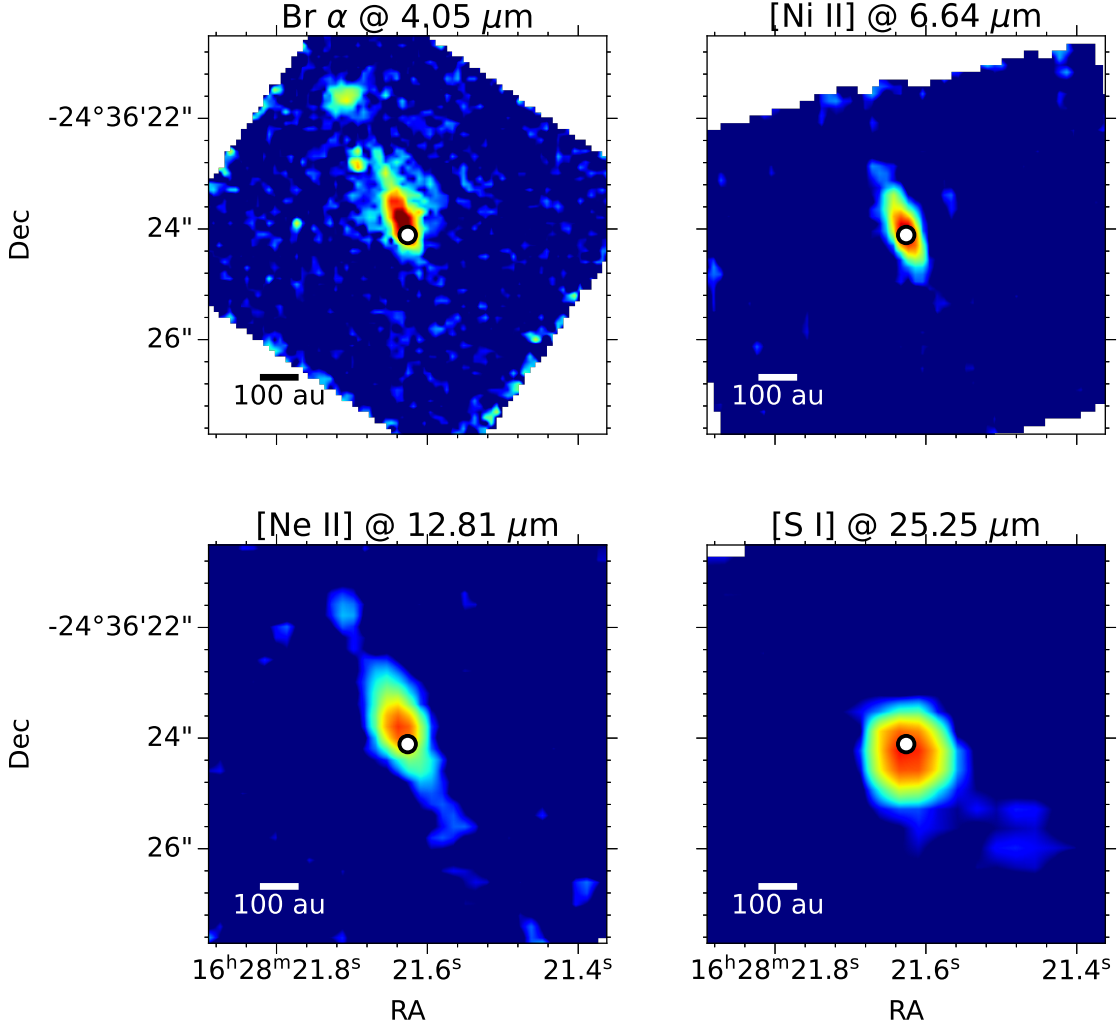


**Figure 3.** The morphology Br- $\alpha$  line and the other atomic fine structure lines and detected towards IRAS 16253-2429. All images are cropped to the same spatial scale. The white solid circle is the MIRI MRS  $14 \mu\text{m}$  continuum position. The scale bar corresponding to 100 au is shown in the bottom right corner.

ing atomic jets, molecular outflows, and envelope cavity structures at spatial scales down to 30 au. In Figure 1, we present a comparison between the Spitzer IRAC (IRAC 1, 2, and 4; Figure 1 a) observations of the protostar, covering a field of view of  $2' \times 2'$ , and the NIRSpec IFU + MIRI MRS observations (Figure 1 b) focused within the inner  $7''$  (also see Federman et al. 2023b). Figure 1 (a) shows the full spatial extent of the protostellar outflow from IRAS 16253-2429 as seen by Spitzer. The black rectangle shows the field of view of the JWST observations. Figure 1(b) shows the zoomed-in inner  $\sim 6''$  region of the protostar as observed with JWST. The  $4.17 \mu\text{m}$  continuum emission is primarily the scattered light from the central source and is shown in red;

it traces the extent of the outflow cavity carved out of the envelope. The molecular outflow traced by  $\text{H}_2$  0-0 S(11) emission at  $4.18 \mu\text{m}$  is shown in green. The atomic jet seen in the  $[\text{Fe II}]$  at  $5.34 \mu\text{m}$  line is shown in blue. The JWST observations reveal that IRAS 16253-2429 exhibits the distinctive “wasp-waist” shape (Barsony et al. 2010), even within the inner  $6''$  region surrounding the protostar. Figure 1(b) further shows that the scattered light cavity is much broader than the molecular emission from  $\text{H}_2$  (also see Federman et al. 2023b and Narang et al. in prep).

The wavelength range covered by the MIRI MRS and NIRSpec IFU instruments encompasses several fine structure lines, including multiple lines of  $[\text{Fe II}]$ . In

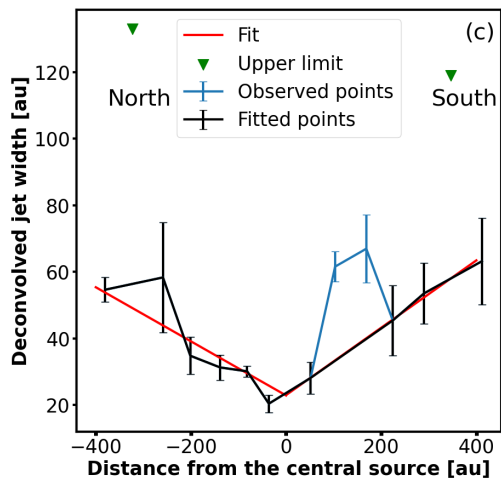
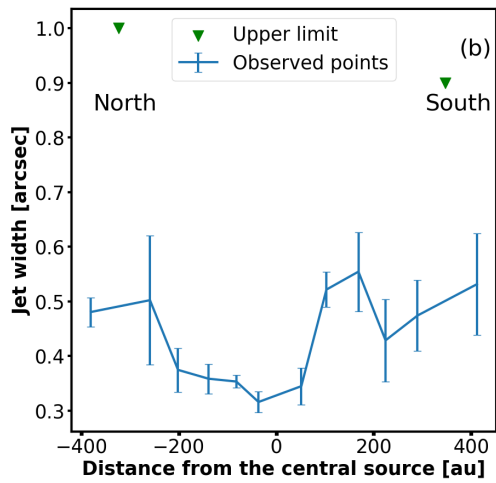
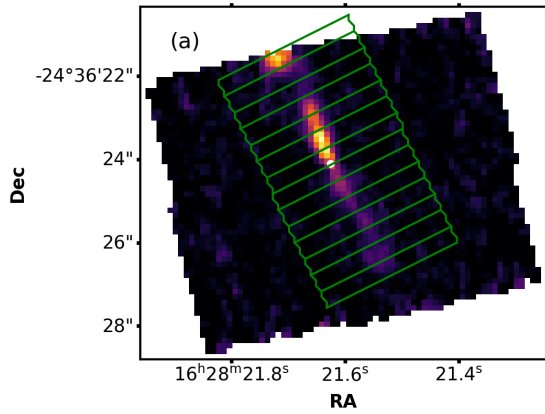


**Figure 4.** (a) The horizontal slices in green marked on top of the jet traced in [Fe II] at  $5.34 \mu\text{m}$ . The white circle represents the protostellar position. (b) The width (FWHM) of the jet as a function of distance from the central protostar. The negative distance corresponds to the northern side, and the positive distance corresponds to the southern side. (c) The deconvolved width (FWHM) of the jet as a function of distance from the central protostar. The fit to the jet width as a function of distance is shown as the red solid line. The green triangles in sub figure (b) and (c) show the upper limits to the width at those points.

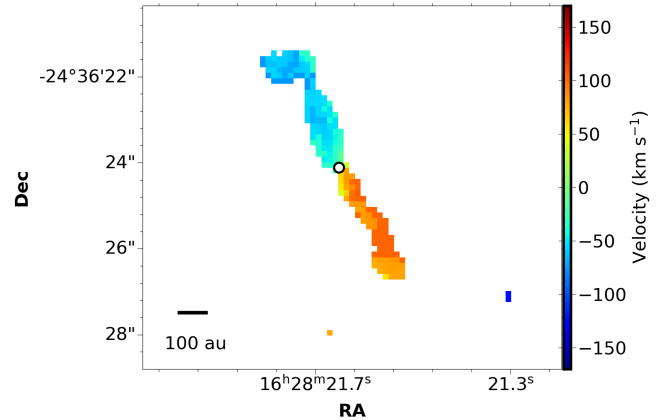


**Figure 5.** The moment 1 map for the [Fe II] line at  $5.34 \mu\text{m}$ . The white solid circle is the MIRI MRS  $14 \mu\text{m}$  continuum position. The scale bar corresponding to 100 au is shown in the bottom left corner.

Figure 2, we present the line maps of all the detected [Fe II] lines observed towards IRAS 16253-2429. These [Fe II] lines trace a highly collimated jet originating from the central protostar. This is the first time (at any wavelength) that a collimated jet has been detected from IRAS 16253-2429. The jet appears brighter on the northern side and weaker to the south; but, this is because of the relatively higher line-of-sight extinction toward the southern cavity (see Section 3.4).

We further find that there are knots at both ends of the jet (see Figure 2) at around 400 au from the central protostar (also see Federman et al. 2023b). The southern knot is best detected in the [Fe II] line at  $5.34 \mu\text{m}$ , with a tentative detection in the [Fe II] lines at  $17.936 \mu\text{m}$  and  $25.988 \mu\text{m}$ . The northern knot is clearly seen in five of the six [Fe II] line maps presented in Figure 2, although it is not fully mapped in the  $5.34 \mu\text{m}$  line, and is only faintly seen in the  $24.5 \mu\text{m}$  line. If we draw a line from the central protostar to the northern- and southern-most knots we find that the jet seen in [Fe II] at  $5.34 \mu\text{m}$  does not fall on this line. The northern knot is clearly offset to the east from the axis of the rest of the northern jet. We also find that the jet has a slight curvature, suggesting that it might be precessing (also see Barsony et al. 2010).

In Figure 3, we present maps of other atomic fine-structure (FS) lines along with the Br- $\alpha$  line at  $4.052 \mu\text{m}$ . We find that the FS lines of [Ne II] at  $12.81 \mu\text{m}$  and the [Ni II] at  $6.64 \mu\text{m}$  also trace the jet seen in [Fe II]. The [Ne II] jet also shows faint knots at both ends similar to the [Fe II] jets. The [S I] emission at  $25.25 \mu\text{m}$ , however, is concentrated on the protostar and does not appear to trace the jet (see Figure 3). The Br- $\alpha$  line observed with NIRSpect appears to trace the

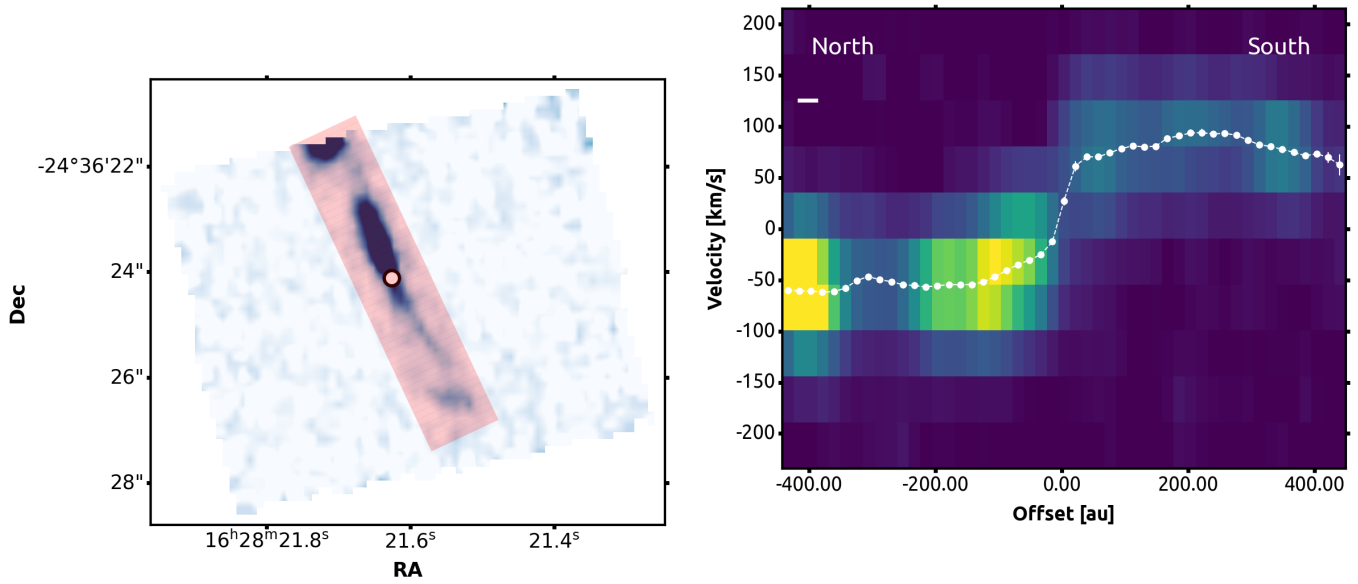


**Figure 6.** (left) The [Fe II] jet at  $5.34 \mu\text{m}$  shown in blue overlaid with a red rectangle encompassing the region used for making the PV diagram. (right) The PV diagram for the [Fe II] line at  $5.34 \mu\text{m}$ . The white circles represent the center of the Gaussian fit to the velocity channels, while the error bars represent the FWHM of the Gaussian fit. The white bar in the top left corner is the PSF of the JWST MIRI at  $5.34 \mu\text{m}$ , which is  $39.2 \text{ au}$  ( $0.28''$ ).

jet and shows the knot on the northern side (see Figure 3). Interestingly, Br- $\alpha$  emission is stronger in the extended jets than at the central source. This suggests that the H I lines observed from protostars via spatially unresolved spectroscopy might have a large contribution due to the jet component; the dominant jet component makes it difficult to isolate emission in this line from accretion flows (see Hartmann et al. 2016; Federman et al. 2023b).

### 3.2. Jet width

Given the high signal-to-noise and high angular resolution at  $5.34 \mu\text{m}$  ( $\sim 0.28''$  Law et al. 2023), it is possible to measure the width of the jet as a function of distance from the protostar. The jet has a position angle of  $23^\circ$  (measured from North towards East). We started by taking slices aligned perpendicular to the jet and averaged them over 3 pixels length along the jet as shown in Figure 4(a). We then fit each of these averaged slices with a Gaussian and the FWHM of the Gaussian is taken as the width of the jet in that slice.

In Figure 4(b) we show the width of the jet (FWHM) as a function of distance from the protostar. As can be seen from Figure 4(b), the protostellar jet appears to expand as we move away from the central protostar. We measure the FWHM of the slices adjacent to the protostar on either side and find the width of the jet

close to the central protostar to be  $\sim 0.33 \pm 0.03''$ . This is comparable to the average PSF FWHM of the MIRI MRS at  $5.34 \mu\text{m}$  of  $\sim 0.28''$  (Law et al. 2023).

In Figure 4(c) we show the deconvolved jet widths (obtained by subtracting out the MIRI MRS PSF FWHM in quadrature) as a function of distance from the central protostar. From a linear fit to the jet width as a function of distance from the central protostar, we obtain the opening angle  $\Theta$  ( $= \text{slope}/2$ ) as well as the jet width at the central position (zero intercept). We find that the average slope of the fit is  $0.09 \pm 0.02$ , corresponding to an opening angle of  $2.6 \pm 0.5^\circ$ . The jet width extrapolated to the source position is  $23 \pm 4 \text{ au}$ , which we take as an upper limit on the jet width at the source location. Federman et al. (2023b) used the NIRSpc observation of the [Fe II] line at  $4.88 \mu\text{m}$  to measure the deconvolved width of the jet from IRAS 16253-2429 at its brightest position. They found a deconvolved jet width to be  $0.144''$  which corresponds to  $\sim 20.2 \text{ au}$

### 3.3. Velocity structure in the jet

In order to explore the velocity structures within the jet, we first constructed a moment 1 map of the [Fe II] line at  $5.34 \mu\text{m}$  as shown in Figure 5. The moment 1 map gives us the intensity-weighted velocity and is an excellent diagnostic tool for understanding the kinematic structures within the jets. As can be seen from Fig-



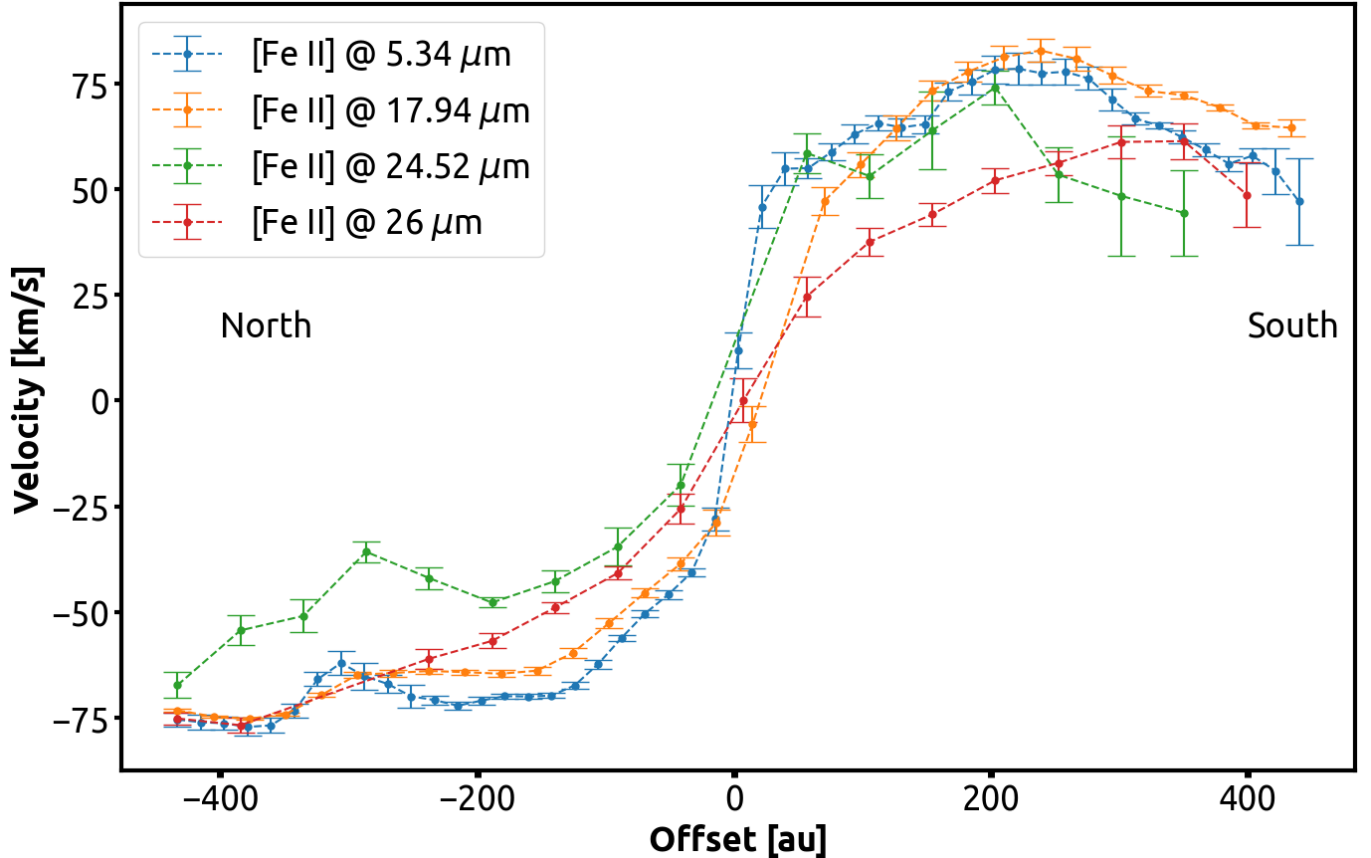


**Figure 7.** The PV diagrams of the observed [Fe II] lines aligned to a common average velocity.

ure 5, the northern part of the jet is blue-shifted with respect to the average velocity, while the southern jet is red-shifted. We note that the velocity of the jet on both sides is fairly constant and the maximum blueshift and redshift velocity difference is  $\sim 130 \text{ km s}^{-1}$ . This is much larger than the systemic cloud velocity of  $\sim 4 \text{ km s}^{-1}$  (Aso et al. 2023). We assume the latter as  $V_{\text{LSR}}$ .

To further investigate the velocity structure of the jet, we constructed a Position-Velocity (PV) diagram, specifically for the [Fe II] line at  $5.34 \mu\text{m}$ . In order to capture the full range of velocities, we carefully selected a rectangular region around the protostar that is both wide and long enough to encompass the entire jet, as illustrated in Figure 6 (a). We show the PV diagram for the [Fe II] line at  $5.34 \mu\text{m}$  in Figure 6 (b). From the PV diagram, it is apparent that as we move away from the central protostar (the driving source of the jet), the velocities on either sides of the jet remain more or less constant. This is similar to what we found with the moment 1 map of [Fe II] at  $5.34 \mu\text{m}$  (see Figure 5) as well. However, within the inner region covering approximately 50 au, we witness rapid changes in velocity.

We also constructed PV diagrams for the various other [Fe II] lines. We computed the velocity of each slice of the spectral cube by converting the wavelength shift with respect to the lab wavelengths (Koo et al. 2016; Tayal & Zatsarinny 2018) to a velocity shift. In Figure 7, we show PV diagrams of all the [Fe II] lines that we have detected from IRAS 16253-2429. Initially, the PV diagrams of the various [Fe II] lines did not align well since uncertainties in the wavelength calibration can introduce offsets of as large as  $40 \text{ km s}^{-1}$  even within a single channel (Argyriou et al. 2023). In Figure 7 we align the velocities in the PV diagrams by setting the mean velocity of the jet seen in each line to zero. It can be seen from Figure 7 that the jets display approximately symmetric velocities with respect to the central protostar. The difference in the peak positive and negative velocities for all the [Fe II] jets are similar, with an average value of  $148 \pm 12 \text{ km s}^{-1}$ . This consistency in peak jet velocities seen in different [Fe II] lines reinforces the notion of a coherent jet structure originating from the central protostar.

Using the PV diagrams we compute the jet velocity as half of the average peak-to-peak velocity. The average peak-to-peak velocity is  $148 \pm 12 \text{ km s}^{-1}$ , which gives

the radial jet velocity as  $74 \pm 6 \text{ km s}^{-1}$ . After correcting for the inclination of the jet using the measured inclination angle of  $64.1 \pm 0.5^\circ$  from Aso et al. (2023), we obtain the peak velocity of the jet to be  $169 \pm 15 \text{ km s}^{-1}$ .

### 3.4. Measuring extinction along the jet

To derive the physical properties of the jet from the observed line maps, we first measure and quantify the line of sight extinction. To determine the spatially varying extinction towards IRAS 16253-2429, we used the molecular  $\text{H}_2$  0-0 S lines. Molecular  $\text{H}_2$  lines have previously been used with Spitzer IRS to determine the extinction values (e.g., Barsony et al. 2010). If we assume that the  $\text{H}_2$  is in local thermodynamical equilibrium (LTE) with an ortho-para ratio of 3 we can construct the rotation diagram for the  $\text{H}_2$  lines (Figure 9 and Figure 11).

In this diagram, the natural logarithm of the column density of  $\text{H}_2$  molecules in the  $J^{\text{th}}$  rotational state,  $N_u$ , divided by the degeneracy of that state ( $g_u$  is the rotational degeneracy equal to  $2J + 1$  and  $g_s$  is the spin degeneracy),  $\ln(N_u/g_u g_s)$ , is plotted as a function of the upper state energy,  $E_u$  (energy of the  $J^{\text{th}}$  rotational state) (see, e.g., Neufeld et al. 2009; Maret et al. 2009; Barsony et al. 2010; Manoj et al. 2013). Assuming that  $\text{H}_2$  emission is optically thin, then the number of  $\text{H}_2$  molecules in the  $J^{\text{th}}$  rotational state is given by:

$$N_u = \frac{4 \pi F_{J,J-1} \lambda_{J,J-1}}{h c A_{J,J-1}} \quad (1)$$

where  $h$ ,  $c$ ,  $F_{J,J-1}$ ,  $\lambda_{J,J-1}$  and  $A_{J,J-1}$  are the Planck's constant, speed of light in vacuum, line flux within the aperture, wavelength, and Einstein A-coefficient, respectively, corresponding to the transition  $J \rightarrow J - 1$ . We can compute an average rotational temperature  $T_{rot}$ , for a relatively small range in  $E_u$  by fitting a straight line to the points in the observed rotational diagram. The negative of the inverse of the slope gives us the  $T_{rot}$ .

Under the LTE assumption, any deviation from this straight line in the narrow range of  $E_u$  is due to extinction. By correcting for these deviations we derive the line of sight extinction towards the protostars. To do so, we can simultaneously fit the rotation diagram and the correction for extinction. We restrict our analysis to  $\text{H}_2$  lines between 6-18  $\mu\text{m}$  (from  $\text{H}_2$  0-0 S(1) to S(6)) to minimize non-LTE effects and also to avoid contamination from molecular CO (also see Rubinstein et al., in prep). We used the extinction law from Klaus Pontopidan (hereafter KP v05; private communication) presented in (Chapman et al. 2009) to derive the extinction towards the protostar (also see section 3.5). We select apertures of radius 0.8'' spaced 1.1'' apart along

the jet (see Figure 8a) and measure the line fluxes within them. We then fit the extinction value  $A_V$  and two rotation temperatures simultaneously, one temperature representing cooler gas between  $\text{H}_2$  0-0 S(1) and S(4) and the other slightly hotter gas between  $\text{H}_2$  0-0 S(3) and S(6)) to the  $\text{H}_2$  0-0 S lines. In Figure 9 we show the  $\text{H}_2$  rotation diagram for aperture 3 (centered on the protostar). We can clearly see how correcting for extinction, especially for the  $\text{H}_2$  S(3) line leads to an improved fit to the temperatures. Figure 11 in the Appendix shows the rest of the  $\text{H}_2$  rotation diagrams. The rotation temperature and  $A_V$  values for different apertures are listed in Table 2.

In Figure 8(b), we show the variation of the line of sight extinction along the length of the jet. We find that the extinction rapidly rises as we move towards the protostar from North to South, attaining a maximum at the protostellar position, after which it remains relatively constant. The details of the  $\text{H}_2$  excitation analysis will be provided in a follow-up paper.

### 3.5. Physical conditions along the jet

We next examined the physical conditions (shock velocity and density) along the jet. We used the 1D shock and photoionization code MAPPINGS V (Sutherland et al. 2018) to model the shock. Furthermore, we used the [Fe II] collisional excitation network from (Tayal & Zatsarinny 2018) instead of the CHIANTI defaults. Our shock models were computed for solar abundance (Asplund et al. 2009) with a frozen-in magnetic field  $B = 15.8 \mu\text{G} \times \sqrt{n/1000 \text{ cm}^{-3}}$ . We implement the full magnetic and UV radiative precursor treatment by iterating and integrating the shock model to convergence.

We chose to use the fine structure lines of [Fe II] and [Ne II] as these lines have the largest extent in the jet. In Figure 10 we have plotted the MAPPINGS shock model grids (nomogram). The predicted ratio of [Ne II] at 12.81  $\mu\text{m}$  and [Fe II] at 5.34  $\mu\text{m}$  in blue runs along the y-axis and is sensitive to the shock velocity ( $v_s$ ) while the predicted ratio of [Fe II] lines at 17.93 and 5.34  $\mu\text{m}$  in green that almost runs along the x-axis is sensitive to the preshock density, ( $\rho_s$ ). By placing the observed line ratios onto this nomogram we can directly read off the shock speed and the preshock density.

We measured the line fluxes along the jet using the same aperture as Figure 8 (left). We placed the dereddened flux ratios for the [Fe II] and [Ne II] lines onto the grid in Figure 10 as colored symbols (the color corresponds to the aperture in Figure 8 (left)) and read off the shock speed and preshock density. We have listed the shock speed and preshock density in Table 2. We find that away from the central protostar the preshock den-

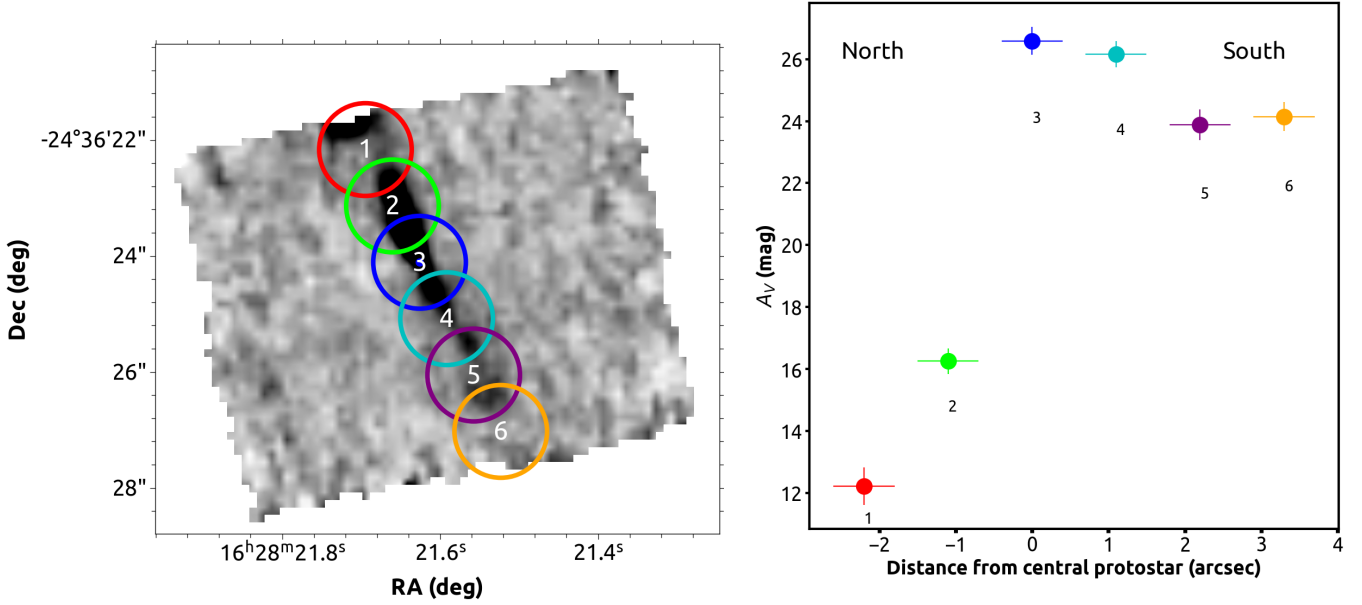


**Figure 8.** (left) The 6 apertures along the jet where we measure the extinction and jet properties. The center of aperture 3 (blue circle) marks the position of the protostar. (right) The measured extinction value along the jet.

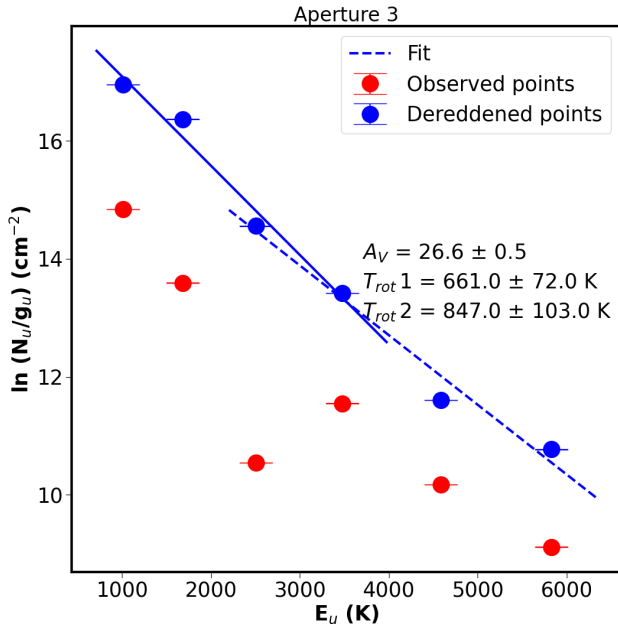


**Figure 9.** The  $H_2$  rotation diagram for aperture 3 (centered on the protostar) in blue. Also shown are the observed points (red) as well as the fit to the dereddened points (blue solid and dashed lines). The extinction value  $A_V$  as well as the rotation temperatures are listed in the Figure.

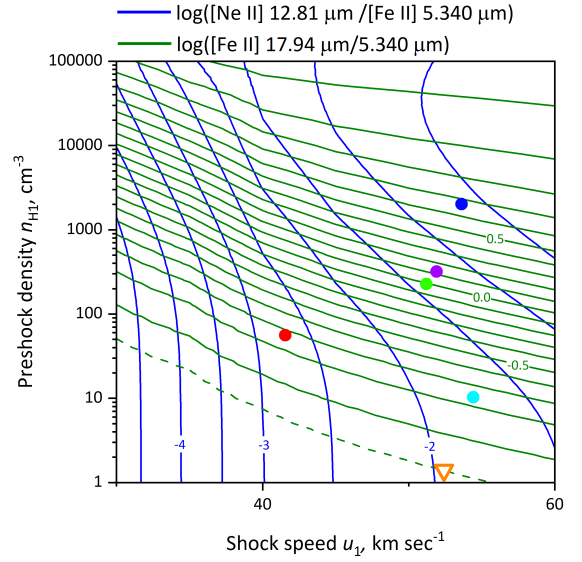


**Figure 10.** The MAPPINGS shock model grid (nomogram) with the extinction corrected ratios for the fine structure lines of [Fe II] and [Ne II]. The ratio of [Ne II] at  $12.81 \mu\text{m}$  and [Fe II] at  $5.34 \mu\text{m}$  in blue runs along the y-axis and is sensitive to the shock velocity while the ratio of [Fe II] lines at  $17.93$  and  $5.34 \mu\text{m}$  in green that almost runs parallel to the x-axis is sensitive to the preshock density. The dashed line is an upper limit to the  $\log([Fe II] 17.936 \mu\text{m} / 5.34 \mu\text{m})$ .

sity rapidly falls, while the shock speed remains roughly constant.

The mass loss rate from the protostar  $\dot{M}_{out}$  can be expressed in terms of the pre-shock density, velocity of the gas entering the shock, and jet radius as:

$$\dot{M}_{out} = \pi \times R^2 \times \rho_s v \times m_H \quad (2)$$

where  $R$  is the radius of the jet,  $\rho_s$  is the pre-shock density,  $v$  is the velocity of the gas entering the shock, and  $m_H$  is the mass of the hydrogen atom. We have also measured the velocity of the shocked gas ( $v_{jet}$ ) in internal working surfaces using the PV diagrams. Based on different jet models the velocity of gas  $v$  can either be the bulk velocity of the jet as derived from the PV diagram ( $v = v_{jet}$ ) (e.g., pulsating jet models of Raga et al. 1990; Raga & Kofman 1992) or the sum of the shock velocity and the jet velocity ( $v = v_{jet} + v_s$ ) (e.g., Rubinstein et al. 2023).

Using the pre-shock density and shock speed derived from the shock grid as well as the jet velocity derived from the PV diagram, and assuming that the jet has a cylindrical cross-section with radius equal to half the jet width measured at the location, we have computed the mass loss rate along the jet from the protostar. The mass loss rate for the various apertures is listed in Table 2. We find that the upper limit to the mass loss rate  $\dot{M}_{out}$  from the central protostar is  $1.1 \times 10^{-10} M_\odot/\text{yr}$ .

In computing the mass loss rate  $\dot{M}_{out}$  from the protostar, the largest uncertainty is not due to any measurement uncertainties, but due to the uncertainty in the adopted extinction law. Chapman et al. (2009) have shown that the extinction law measured towards molecular clouds is highly variable and not only depends upon the molecular cloud but also the environment. To quantify the effects of using different extinction laws on our results, we repeated our analysis of computing extinction and estimating the mass loss rate using two additional extinction laws, that of McClure (2009) and Hensley & Draine (2021). We compute the mass loss rate from the central protostar at the base of the jet (from aperture 3) assuming  $v = v_{jet} + v_s$ . We find that the mass loss rate obtained using the extinction law from McClure (2009) is  $4.2 \times 10^{-11} M_\odot \text{ yr}^{-1}$  and using Hensley & Draine (2021) is  $3.2 \times 10^{-11} M_\odot \text{ yr}^{-1}$ . These  $\dot{M}_{out}$  values and the ones listed in Table 2 (for aperture 3) are within a factor of 3.5, indicating that the upper limit that we obtain for mass loss rate,  $\dot{M}_{out} \leq 1.1 \times 10^{-10}$  is robust.

#### 4. DISCUSSION

Our JWST observations reveal a highly collimated atomic jet in the IR fine structure lines and H I lines

from the low luminosity and very low mass protostar IRAS 16253-2429. No collimated molecular jet is detected, and although IR H<sub>2</sub> emission is detected along the outflow cavity, it has much wider opening angle and does not spatially follow the collimated atomic jet. The jet seen in the FS lines appears brighter on the blueshifted north-eastern side that is facing us, and is fainter to the south-west; this is due to the higher line-of-sight extinction toward the south-western cavity (see from Figure 8).

The jets on either side appear to have similar velocities that more or less remain constant as a function of distance from the driving source. The jet velocity, corrected for inclination effects (using the inclination of 64.1°), is  $169 \pm 15 \text{ km s}^{-1}$ . The collimated jet seen in the JWST line images extends up to about 400 au (see Figure 7; 916 au after correcting for inclination) from the driving source on either side. This implies a dynamical timescale of  $\sim 26 \text{ yr}$ , suggesting that the jet seen in the JWST IFUs was ejected only in the last 26 yr.

The width of the jet (FWHM) at the base is marginally resolved and is  $\sim 23 \pm 4 \text{ au}$ , and the jet tends to widen as it moves away from the central source with an opening angle  $\Theta = 2.6^\circ$ . If the jet is ballistically confined, then the opening angle can be expressed as a ratio of the sound speed within the jet and the jet speed.

$$\Theta = \frac{c_s}{v_{jet}} \quad (3)$$

where  $v_{jet}$  is the jet velocity of  $169 \pm 15 \text{ km s}^{-1}$  and  $c_s$  is the sound speed. If we assume that the shock temperature is 10,000 K (e.g., Ray & Ferreira 2021) then the sound speed  $c_s = 10 \text{ km s}^{-1}$ , which gives an opening angle of  $3.4 \pm 0.3^\circ$ . This is roughly consistent with the opening angle we measure from the observed jet widths. This suggests that the jet is likely ballistically confined, at least within the central  $\lesssim 1000 \text{ au}$  of the driving source; other confinement mechanisms, however, could be at play at larger distances.

The physical conditions of the jet derived from our analysis indicate shock velocities of  $42\text{--}54 \text{ km s}^{-1}$  from the base to one end of the jet, suggesting that there is no significant acceleration along the jet. The preshock densities estimated are in the range of  $\sim 10\text{--}2000 \text{ cm}^{-3}$ , indicating that the jet is rather tenuous.

The mass loss rate measured from the central protostar is  $\dot{M}_{out} \leq 1.1 \times 10^{-10} M_\odot \text{ yr}^{-1}$ . Even when different extinction laws are used, the mass loss rate changes only by a factor of 3.5 or so. The estimated mass loss rate appears low, even for a very low mass protostar. The simultaneous accretion rate derived from the OH lines in the MIRI spectrum of IRAS 16253-2429

**Table 2.** The extinction  $A_V$ , the rotation temperature of the  $H_2$  gas ( $T_{rot1}$  and  $T_{rot2}$ ), the shock velocities, preshock densities, jet radius  $R$  (computed using the opening angle  $\Theta$  and the jet width at the base) along with the mass outflow rate  $\dot{M}_{out}$  for each of the apertures shown in Figure 8. <sup>b</sup>

Aperture	Distance from Protostar (")	$A_V$	$T_{rot1}$ (K)	$T_{rot2}$ (K)	$v_s$ (km s <sup>-1</sup> )	$\rho_s$ (cm <sup>-3</sup> )	$R$ (au)	$\dot{M}_{out}$ for $v = v_{jet} + v_s$ ( $M_\odot$ yr <sup>-1</sup> )	$\dot{M}_{out}$ for $v = v_{jet}$ ( $M_\odot$ yr <sup>-1</sup> )
1*	-2.2	$12.3 \pm 0.6$	$526 \pm 34$	$794 \pm 65$	>42	$>6 \times 10^1$	25.3	$>1.5 \times 10^{-11}$	$>1.2 \times 10^{-11}$
2	-1.1	$16.2 \pm 0.4$	$585 \pm 41$	$873 \pm 87$	51	$2 \times 10^2$	18.4	$2.8 \times 10^{-11}$	$2.1 \times 10^{-11}$
3	0	$26.6 \pm 0.5$	$661 \pm 72$	$847 \pm 103$	54	$2 \times 10^3$	11.5	$1.1 \times 10^{-10}$	$8 \times 10^{-11}$
4	1.1	$26.1 \pm 0.4$	$685 \pm 60$	$852 \pm 93$	52	$3 \times 10^2$	18.4	$4.2 \times 10^{-11}$	$3.2 \times 10^{-11}$
5	2.2	$23.9 \pm 0.4$	$622 \pm 55$	$840 \pm 83$	54	$1 \times 10^1$	25.3	$2.7 \times 10^{-12}$	$2 \times 10^{-12}$
6	3.3	$24.2 \pm 0.4$	$672 \pm 51$	$882 \pm 108$	52	< 2	32.3	$<8.6 \times 10^{-13}$	$<6.6 \times 10^{-13}$

<sup>a</sup> \* Aperture 1 is a lower limit due to the fact that the northern knot is not entirely covered by the MIRI channel-1 FOV.

<sup>b</sup> \* Aperture 1 is a lower limit due to the fact that the northern knot is not entirely covered by the MIRI channel-1 FOV.

is  $\dot{M}_{acc} \sim 1.3 \times 10^{-9} M_\odot \text{ yr}^{-1}$  (Watson et al. in prep), commensurate with the low mass loss rate observed. The protostar appears to be going through a phase of low mass accretion/ejection currently. It is, however, driving a highly collimated jet, even while in the relatively quiet phase, suggesting that collimated jets are present even when protostars are passing through a low accretion phase (also see Aso et al. 2023).

Although the protostar IRAS 16253-2429 is currently in a quiescent phase, it must have gone through earlier epochs of high mass accretion/ejection, and is also very likely to go through active high accretion phase later in its life, for the following reasons.

The current mass of the central source based on the ALMA observations of the Keplerian disk is about  $0.15 M_\odot$  (Aso et al. 2023). At the current mass accretion rate, it would take more than 100 Myr to accrete a mass of  $0.15 M_\odot$ . IRAS 16253-2429 is a Class 0 protostar, which is likely to be  $\ll 1$  Myr old (e.g., Dunham et al. 2014), suggesting that the protostar must have had a period of much higher accretion rate at an earlier stage during which most of the current mass was accreted. Additionally, wide cavities are already present in the envelope of IRAS 16253-2429 (see Federman et al. 2023b), which must have been carved out by powerful jets and outflows associated with an earlier high accretion phase. All these evidence indicate that IRAS 16253-2429 must have been accreting at a significantly higher rate at an earlier time in its life. Zakri et al. (2022) have shown that during these high accretion phases, the protostar can accrete as much as 100% of its current mass.

The envelope mass of IRAS 16253-2429 estimated from mm observations is in the range of  $0.2$  to  $1 M_\odot$  (Stanke et al. 2006; Enoch et al. 2008; Tobin et al. 2011) depending on the size of the core considered, the opac-

ity values used, and the assumed dust temperature. All measurements and our modeling efforts are consistent with a mass of  $\gg 0.2 M_\odot$  within an envelope radius of  $\sim 4200$  au, suggesting that there is significantly more mass in the envelope of IRAS 16253-2429 than in the central object. Given the available mass in the envelope, it is reasonable to assume that at least an additional  $0.15 M_\odot$  will be accreted onto the central source. This would make the final mass of IRAS 16253-2429 to be  $\sim 0.3 M_\odot$ , which is where the stellar initial mass function peaks (Bastian et al. 2010).

At the current accretion rate, it would take  $> 100$  Myr to accrete this mass, strongly suggesting that the protostar will again go into a high mass accretion/ejection phase. This is consistent with the results of Zakri et al. (2022), who find that Class 0 protostars undergo bursts every few hundred years that last only a few decades; hence it is more likely that a protostar is observed in between bursts. In the case of one Class 0 protostar, HOPS 383, the pre and post-burst periods are characterized by a quiescence with a very low accretion rate (Zakri et al. 2022). Our JWST observations appear to have captured IRAS 16253-2429 during the interlude between the accretion bursts, i.e. in the quiescent phase, and yet driving a tenuous but highly collimated jet.

The low mass loss rate that we derive for the protostar is also consistent with the non-detection of the molecular jet from the source. Tabone et al. (2020) have argued that self-shielding of the jet from FUV photons generated from the central source or from shocks along the jet requires much higher mass loss rates from the protostar.

## 5. SUMMARY AND CONCLUSIONS

In this work, we report the discovery of a highly collimated jet in multiple [Fe II], other fine structure lines, an H I originating from the Class 0 protostar IRAS 16253-2429, the least luminous (and least massive) source in the Investigating Protostellar Accretion (IPA) program. No collimated molecular jet is detected in CO, SiO or H<sub>2</sub> in the IR with JWST and in the (sub-)mm with ALMA. We determine the following properties of the jets/outflows:

1. The jet (as seen in [Fe II] line at 5.34  $\mu\text{m}$ ) is  $23 \pm 4$  au wide at the base with an opening angle of  $2.6 \pm 0.5^\circ$ .
2. Based on our analysis of the PV diagram of various [Fe II] lines, we find that the jet has a velocity of  $169 \pm 15 \text{ km s}^{-1}$  (after correcting for inclination). The jets on either side of the protostar appear to have similar velocities that remain almost constant as a function of distance from the center.
3. We determine the line of sight extinction  $A_V$  along the jet using H<sub>2</sub> lines in the cavity, which gives  $A_V$  values ranging from  $\sim 12$  to  $\sim 27$ .
4. Using the extinction corrected flux ratios of [Ne II] at 12.81  $\mu\text{m}$  and the [Fe II] lines at 5.34  $\mu\text{m}$  and 17.936  $\mu\text{m}$ , we derive a shock velocity of  $54 \text{ km s}^{-1}$  and a preshock density of  $2.0 \times 10^3 \text{ cm}^{-3}$  at the base of the jet.
5. Assuming a cylindrical jet with a cross-sectional width of 23 au and using the jet velocity of  $169 \text{ km s}^{-1}$  along with the derived preshock density and shock velocity, we compute the mass

loss rate from the jet to be between  $0.32\text{--}1.1 \times 10^{-10} M_\odot \text{ yr}^{-1}$ .

The low mass loss rate derived is consistent with simultaneous measurements of low accretion rate of  $\lesssim 10^{-9} M_\odot \text{ yr}^{-1}$  for IRAS 16253-2429 (Watson et al. in prep), indicating that the protostar is likely in the quiescent accretion phase. Our results show that even a very low mass protostar in a quiescent phase with low accretion rate can still drive a highly collimated jet.

## 6. ACKNOWLEDGMENT

This work is based on observations made with the NASA/ESA/CSA James Webb Space Telescope. The data were obtained from the Mikulski Archive for Space Telescopes at the Space Telescope Science Institute, which is operated by the Association of Universities for Research in Astronomy, Inc., under NASA contract NAS 5-03127 for JWST. These observations are associated with program #1802. Support for SF, AER, STM, RG, WF, JG, JJT and DW in program #1802 was provided by NASA through a grant from the Space Telescope Science Institute, which is operated by the Association of Universities for Research in Astronomy, Inc., under NASA contract NAS 5-03127. A.C.G. has been supported by PRIN-MUR 2022 20228JPA3A “The path to star and planet formation in the JWST era (PATH)” and by INAF-GoG 2022 “NIR-dark Accretion Outbursts in Massive Young stellar objects (NAOMY)”. G.A. and M.O., acknowledge financial support from grants PID2020-114461GB-I00 and CEX2021-001131-S, funded by MCIN/AEI/10.13039/501100011033.

*Facility:* JWST (NIRSpec, MIRI)

## APPENDIX

### A. ROTATION DIAGRAM ALONG THE JET

## REFERENCES

- Ray, T. P. & Ferreira, J. 2021, *NewAR*, 93, 101615. doi:10.1016/j.newar.2021.101615
- Hensley, B. S. & Draine, B. T. 2021, *ApJ*, 906, 73. doi:10.3847/1538-4357/abc8f1
- Law, D. D., Morrison, J. E., Argyriou, I., et al. 2023, *AJ*, 166, 45. doi:10.3847/1538-3881/acdddc
- Khanzadyan, T., Gredel, R., Smith, M. D., et al. 2004, *A&A*, 426, 171. doi:10.1051/0004-6361:20041241
- Chapman, N. L., Mundy, L. G., Lai, S.-P., et al. 2009, *ApJ*, 690, 496. doi:10.1088/0004-637X/690/1/496
- Barsony, M., Wolf-Chase, G. A., Ciardi, D. R., et al. 2010, *ApJ*, 720, 64. doi:10.1088/0004-637X/720/1/64
- Dunham, M. M., Crapsi, A., Evans, N. J., et al. 2008, *ApJS*, 179, 249. doi:10.1086/591085
- Stanke, T., Smith, M. D., Gredel, R., et al. 2006, *A&A*, 447, 609. doi:10.1051/0004-6361:20041331
- Tobin, J. J., Hartmann, L., Chiang, H.-F., et al. 2011, *ApJ*, 740, 45. doi:10.1088/0004-637X/740/1/45
- Zucker, C., Speagle, J. S., Schlafly, E. F., et al. 2020, *A&A*, 633, A51. doi:10.1051/0004-6361/201936145

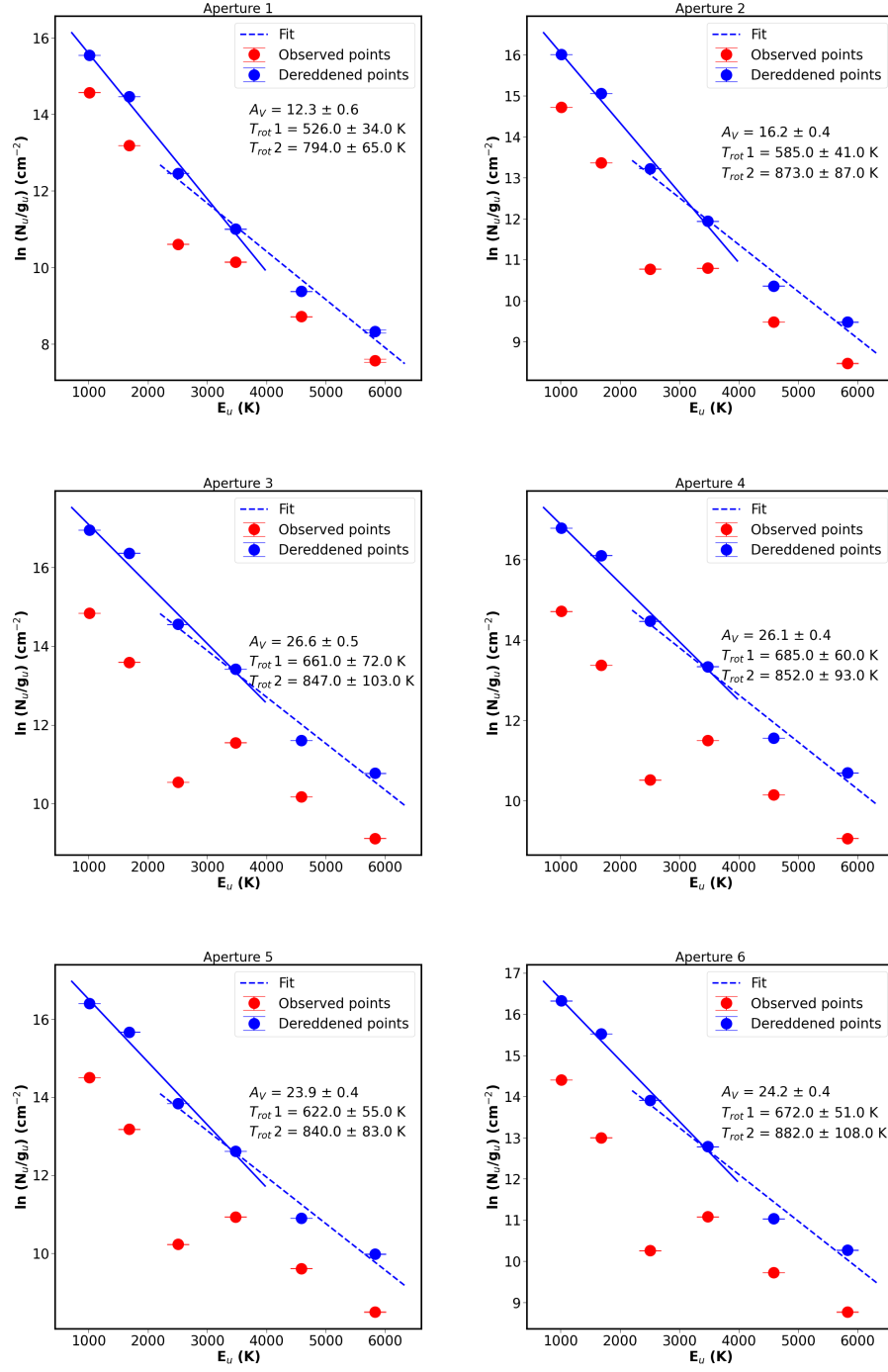


**Figure 11.** The H<sub>2</sub> rotation diagram for all aperture as shown in Figure 8. Also shown are the observed points (red) as well as the fit to the dereddened points (blue solid and dashed lines). The extinction value  $A_V$  as well as the rotation temperatures are listed in the figure.

- Hsieh, T.-H., Hirano, N., Belloche, A., et al. 2019, *ApJ*, 871, 100. doi:10.3847/1538-4357/aaf4fe
- Yen, H.-W., Koch, P. M., Takakuwa, S., et al. 2017, *ApJ*, 834, 178. doi:10.3847/1538-4357/834/2/178
- Rieke, G. H., Wright, G. S., Böker, T., et al. 2015, *PASP*, 127, 584. doi:10.1086/682252
- Wright, G. S., Wright, D., Goodson, G. B., et al. 2015, *PASP*, 127, 595. doi:10.1086/682253
- Jakobsen, P., Ferruit, P., Alves de Oliveira, C., et al. 2022, *A&A*, 661, A80. doi:10.1051/0004-6361/202142663
- Böker, T., Arribas, S., Lützgendorf, N., et al. 2022, *A&A*, 661, A82. doi:10.1051/0004-6361/202142589
- Shang, H., Li, Z.-Y., & Hirano, N. 2007, *Protostars and Planets V*, 261
- Pudritz, R. E., Ouyed, R., Fendt, C., et al. 2007, *Protostars and Planets V*, 277. doi:10.48550/arXiv.astro-ph/0603592
- Watson, D. M., Calvet, N. P., Fischer, W. J., et al. 2016, *ApJ*, 828, 52. doi:10.3847/0004-637X/828/1/52
- Najita, J. R. & Shu, F. H. 1994, *ApJ*, 429, 808. doi:10.1086/174365
- Wardle, M. & Koenigl, A. 1993, *ApJ*, 410, 218. doi:10.1086/172739
- Shu, F., Najita, J., Ostriker, E., et al. 1994, *ApJ*, 429, 781. doi:10.1086/174363
- Shu, F. H., Lizano, S., Ruden, S. P., et al. 1988, *ApJL*, 328, L19. doi:10.1086/185152
- Salmeron, R., Königl, A., & Wardle, M. 2011, *MNRAS*, 412, 1162. doi:10.1111/j.1365-2966.2010.17974.x
- Asplund, M., Grevesse, N., Sauval, A. J., et al. 2009, *ARA&A*, 47, 481. doi:10.1146/annurev.astro.46.060407.145222
- Sutherland, R., Dopita, M., Binette, L., et al. 2018, *Astrophysics Source Code Library*. ascl:1807.005
- Tayal, S. S. & Zatsarinny, O. 2018, *PhRvA*, 98, 012706. doi:10.1103/PhysRevA.98.012706
- Megeath, T., Anglada, G., Atnagulov, P., et al. 2021, *JWST Proposal*. Cycle 1, 1802
- Hartmann, L., Herczeg, G., & Calvet, N. 2016, *ARA&A*, 54, 135. doi:10.1146/annurev-astro-081915-023347
- Fall, S. M., Krumholz, M. R., & Matzner, C. D. 2010, *ApJL*, 710, L142. doi:10.1088/2041-8205/710/2/L142
- Shu, F. H., Najita, J. R., Shang, H., et al. 2000, *Protostars and Planets IV*, 789
- Blandford, R. D. & Payne, D. G. 1982, *MNRAS*, 199, 883. doi:10.1093/mnras/199.4.883
- Pudritz, R. E. & Norman, C. A. 1983, *ApJ*, 274, 677. doi:10.1086/161481
- Frank, A., Ray, T. P., Cabrit, S., et al. 2014, *Protostars and Planets VI*, 451. doi:10.2458/azu\_uapress.9780816531240-ch020
- Lee, C.-F., Tabone, B., Cabrit, S., et al. 2021, *ApJL*, 907, L41. doi:10.3847/2041-8213/abda38
- Spruit, H. C. 1996, *Evolutionary Processes in Binary Stars*, 477, 249
- Manoj, P., Watson, D. M., Neufeld, D. A., et al. 2013, *ApJ*, 763, 83. doi:10.1088/0004-637X/763/2/83
- Matsushita, Y., Takahashi, S., Machida, M. N., et al. 2019, *ApJ*, 871, 221. doi:10.3847/1538-4357/aaf1b6
- Enoch, M. L., Evans, N. J., Sargent, A. I., et al. 2008, *ApJ*, 684, 1240. doi:10.1086/589963
- Maret, S., Bergin, E. A., Neufeld, D. A., et al. 2009, *ApJ*, 698, 1244. doi:10.1088/0004-637X/698/2/1244
- Neufeld, D. A., Nisini, B., Giannini, T., et al. 2009, *ApJ*, 706, 170. doi:10.1088/0004-637X/706/1/170
- Agra-Amboage, V., Cabrit, S., Dougados, C., et al. 2014, *A&A*, 564, A11. doi:10.1051/0004-6361/201220488
- McClure, M. 2009, *ApJL*, 693, L81. doi:10.1088/0004-637X/693/2/L81
- Bate, M. R. 2009, *MNRAS*, 392, 1363. doi:10.1111/j.1365-2966.2008.14165.x
- Bally, J. 2016, *ARA&A*, 54, 491. doi:10.1146/annurev-astro-081915-023341
- Caratti o Garatti, A., Giannini, T., Nisini, B., et al. 2006, *A&A*, 449, 1077. doi:10.1051/0004-6361:20054313
- Yang, Y.-L., Green, J. D., Pontoppidan, K. M., et al. 2022, *ApJL*, 941, L13. doi:10.3847/2041-8213/aca289
- Bastian, N., Covey, K. R., & Meyer, M. R. 2010, *ARA&A*, 48, 339. doi:10.1146/annurev-astro-082708-101642
- Appel, S. M., Burkhardt, B., Semenov, V. A., et al. 2023, *ApJ*, 954, 93. doi:10.3847/1538-4357/ace897
- Hennebelle, P., Commerçon, B., Lee, Y.-N., et al. 2020, *ApJ*, 904, 194. doi:10.3847/1538-4357/abfbab
- Beuther, H., van Dishoeck, E. F., Tychoniec, L., et al. 2023, *A&A*, 673, A121. doi:10.1051/0004-6361/202346167
- Harsono, D., Bjerke, P., Ramsey, J. P., et al. 2023, *ApJL*, 951, L32. doi:10.3847/2041-8213/acdfca
- Reipurth, B., Davis, C. J., Bally, J., et al. 2019, *AJ*, 158, 107. doi:10.3847/1538-3881/ab2d25
- Pelletier, G. & Pudritz, R. E. 1992, *ApJ*, 394, 117. doi:10.1086/171565
- Matt, S. & Pudritz, R. E. 2005, *ApJL*, 632, L135. doi:10.1086/498066
- Matt, S. & Pudritz, R. E. 2008, *ApJ*, 678, 1109. doi:10.1086/533428
- Aso, Y., Kwon, W., Ohashi, N., et al. 2023, *ApJ*, 954, 101. doi:10.3847/1538-4357/ace624
- Lee, C.-F. 2020, *A&A Rv*, 28, 1. doi:10.1007/s00159-020-0123-7
- Raga, A. C., Canto, J., Binette, L., et al. 1990, *ApJ*, 364, 601. doi:10.1086/169443



- Raga, A. C. & Kofman, L. 1992, *ApJ*, 386, 222.  
doi:10.1086/171008
- Podio, L., Tabone, B., Codella, C., et al. 2021, *A&A*, 648, A45. doi:10.1051/0004-6361/202038429
- Tabone, B., Godard, B., Pineau des Forêts, G., et al. 2020, *A&A*, 636, A60. doi:10.1051/0004-6361/201937383
- Lee, C.-F., Li, Z.-Y., Shang, H., et al. 2022, *ApJL*, 927, L27. doi:10.3847/2041-8213/ac59c0
- Koo, B.-C., Raymond, J. C., & Kim, H.-J. 2016, *Journal of Korean Astronomical Society*, 49, 109.  
doi:10.5303/JKAS.2016.49.3.109
- Rubinstein, A. E., Karnath, N., Quillen, A. C., et al. 2023, *ApJ*, 948, 39. doi:10.3847/1538-4357/acc401
- Fischer, W. J., Megeath, S. T., Furlan, E., et al. 2017, *ApJ*, 840, 69. doi:10.3847/1538-4357/aa6d69
- Zakri, W., Megeath, S. T., Fischer, W. J., et al. 2022, *ApJL*, 924, L23. doi:10.3847/2041-8213/ac46ae
- Argyriou, I., Glasse, A., Law, D. R., et al. 2023, *A&A*, 675, A111. doi:10.1051/0004-6361/202346489
- Ray, T. P. et al. *Nature* 622, 48–52 (2023).
- Pokhrel, R., Megeath, S. T., Gutermuth, R. A., et al. 2023, *ApJS*, 266, 32. doi:10.3847/1538-4365/acbfac
- Federman, S., Megeath, S. T., Tobin, J. J., et al. 2023, *ApJ*, 944, 49. doi:10.3847/1538-4357/ac9f4b
- Dunham, M. M., Stutz, A. M., Allen, L. E., et al. 2014, *Protostars and Planets VI*, 195.  
doi:10.2458/azu\_uapress\_9780816531240-ch009
- Federman, S., Megeath, S. T., Rubinstein, A. E., et al. 2023, arXiv:2310.03803. doi:10.48550/arXiv.2310.03803
- Narang, M., Puravankara, M., Tyagi, H., et al. 2023, arXiv:2308.12689. doi:10.48550/arXiv.2308.12689